Accepted Manuscript

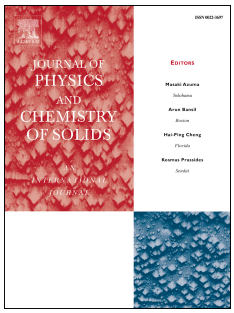

Evaluation of structural, optical and mechanical behaviour of L-argininium bis(trifluoroacetate) single crystal: An efficient organic material for second harmonic generation applications

Sonia, N. Vijayan, Mahak Vij, Harsh Yadav, Ravinder Kumar, Debashish Sur, Budhendra Singh, S.A. Martin Britto Dhas, Sunil Verma

PII: S0022-3697(18)32688-X

DOI: https://doi.org/10.1016/j.jpcs.2019.02.002

Reference: PCS 8900

To appear in: *Journal of Physics and Chemistry of Solids*

Received Date: 5 October 2018

Revised Date: 28 December 2018

Accepted Date: 1 February 2019

Please cite this article as: Sonia, N. Vijayan, M. Vij, H. Yadav, R. Kumar, D. Sur, B. Singh, S.A. Martin Britto Dhas, S. Verma, Evaluation of structural, optical and mechanical behaviour of L-argininium bis(trifluoroacetate) single crystal: An efficient organic material for second harmonic generation applications, *Journal of Physics and Chemistry of Solids* (2019), doi: https://doi.org/10.1016/j.jpcs.2019.02.002.

LABTF Synthesised salt

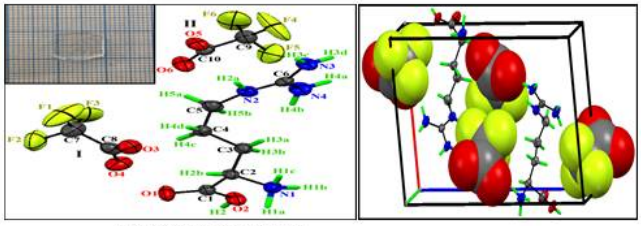

LABTF single crystal

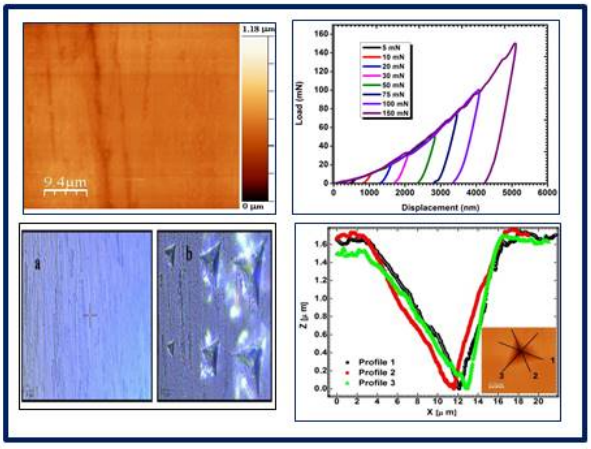

Mechanical behaviour

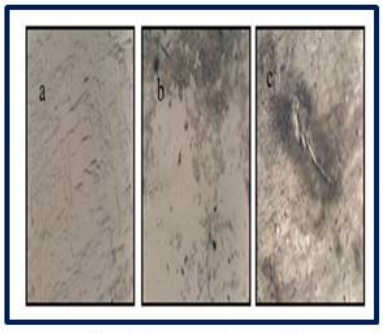

Shock damage threshold

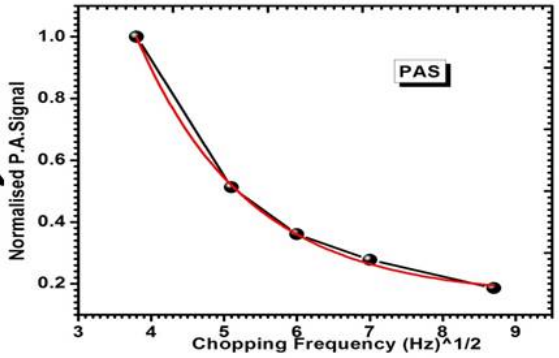

Variation of PA signals

Evaluation of structural, optical and mechanical behaviour of L-argininium bis(trifluoroacetate) single crystal : An efficient organic material for Second Harmonic Generation applications

Sonia[1, 2], N. Vijayan[*, 2], Mahak Vij[1, 2], Harsh Yadav[3], Ravinder Kumar[1,2], Debashish Sur[4], Budhendra Singh[5], S.A.Martin Britto Dhas[6], Sunil Verma[7]

[1]Academy of Scientific and Innovative Research, CSIR – National Physical Laboratory New Delhi –110012, India

[2]CSIR-National Physical Laboratory, Dr. K.S. Krishnan Road, New Delhi – 110 012, India

[3]Crystal Lab, Department of Physics & Astrophysics, University of Delhi

[4]Department of Metallurgy and Materials Engineering, IIEST Shibpur, Howrah – 711103, India

[5]TEMA-NRD, Mechanical Engineering Department and Aveiro Institute of Nanotechnology (AIN), University of Aveiro, 3810-193 Aveiro, Portugal

[6]Department of Physics, Sacred Heart College, Tirupattur, Vellore – 635601, India

[7]Laser Materials Development and Devices Division, Raja Ramanna Centre for Advanced Technology, Indore – 452013, India

Abstract

In the present technologically advanced era, non-linear optical materials especially organic derivatives are in the limelight due to their fast response in electro-optic switches and high nonlinear efficiency. Therefore, with respect to this behaviour, single crystals of L-argininium Bis(trifluoroacetate) (here in after called LABTF) an organic material was grown by slow evaporation solution growth technique. The grown single crystal was subjected to single crystal X-Ray diffractometer to validate its chemical structure and compound formation. The titled compound crystallizes into an asymmetric entity that comprises of one divalent L-argininium cation and two monovalent trifluoroacetic anion. All the intermolecular hydrogen bonds present in the LABTF crystal structure are investigated by 3D molecular Hirshfeld surface analysis and their relative involvements are disintegrated using 2D fingerprint plots. Further, the crystalline perfection assessment was performed using high-resolution X-Ray diffractometer which divulges the absence of structural grain boundaries in the obtained crystal. Thermal transport parameters of the titled compound were measured through Photoacoustic spectroscopy. The shock strength above which the crystal induces damage was found by the shock damage threshold technique. In addition, mechanical property related parameters such as hardness, stiffness and Young's Modulus were evaluated

using the nanoindentation technique. These mechanical parameters resolve the reliability of devices and it can be enhanced by improving the crystal quality.

Keywords: High-resolution X-Ray diffraction, Birefringence, Photoacoustic spectroscopy, Thermal conductivity, Thermal effusivity, Damage threshold, Mechanical Strength, Nanoindentation, Stiffness, Young's Modulus.

***Corresponding Author**

Dr. N. Vijayan, Sr. Scientist

Crystal Growth and X-ray Analysis Section

CSIR-National Physical Laboratory

Dr. K.S. Krishnan Road, New Delhi-110012, INDIA

E-mail: nvijayan@nplindia.org; vjnphy@yahoo.com

Ph. No. +91-11-45608263; FAX No. +91-11-45609310

1. Introduction

For the past few decades, numerous researchers have put their efforts in the development of new and innovative organic non-linear optical (NLO) materials. These compounds have potential to exhibit high nonlinearities, high optical susceptibility, fast response in the electro-optic effect and easiness in device fabrication [1-8]. Because of these traits, the need of such compounds has been increasing day by day for numerous applications such as optical bistability, telecommunications, optical computing, high power lasers and many more [9]. In order to fulfill these demands, it is necessary to develop and grow new organic materials. Owing to π electron conjugated system that contains electron donor group on one side and electron acceptor group on another, a push-pull conjugated structure is created [10-11]. This assists organic compounds to demonstrate second and third order nonlinearity [12-14]. By considering the above-said conditions, amino acids are found to be a suitable candidate for NLO applications because of the presence of carboxyl (-COO) group as a proton donor and amino ($-NH_3$) group as a a proton acceptor in their molecular structure [15]. Apart from its molecular chirality and zwitterionic formation, these compounds have capability to show broad spectra of transmittance under UV and Visible range [16]. Usually, amino acids

crystallize in a non-centrosymmetric crystal system due to its asymmetric nature which is an essential precondition for a second harmonic generation (SHG). There are various examples of organic amino acid-based single crystals like L-arginine 4-nitrophenolate 4-nitrophenol dihydrate, L-arginine paranitrobenzoate monohydrate, L-arginine acetate and many more compounds have been grown and characterized [17-19].

L-arginine is an optically active amino acid that generally presents in the biological system. It shows the flexibility of molecular configuration and also exists in zwitterionic form due to the protonation of both guanidyl and amino group along with deprotonation of carboxylic groups. The doubly charged L-arginine with protonated α-amino and guanidyl groups facilitates formation of several L-arg ·2X (X is different organic and inorganic counterparts) compounds by cationic-anionic interaction [20-21]. Here, the present compound L-argininium Bis(trifluoroacetate) LABTF comes under the same category. It belongs to the monoclinic crystallographic system with $P2_1$ space group [22]. The titled compound is thermally stable up to 215 ºC and its SHG efficiency is comparable with L-arginine trifluoroacetate single crystal [23]. In the present report, slow evaporation solution growth technique was used to grow LABTF single crystals. To confirm the formation of a compound, single crystal XRD studies have been carried out. Crystalline perfection and optical properties were studied using High-Resolution X-Ray Diffractometer (HRXRD), photoluminescence (PL) and birefringence. Further, its mechanical and thermal properties were examined using shock damage threshold, nanoindentation, and photoacoustic spectroscopy to ensure its ability in device fabrications.

2. Experimental

For the growth of single crystal, firstly L-argininium bis(trifluoroacetate) i.e., LABTF salt was synthesized by dissolving the raw material, namely, L-Arginine and Trifluoroacetic acid with a molar ratio of 1:2 in distilled water. The prepared solution was kept on the stirrer at 40 ^{o}C for 4 hours to make a transparent solution. The prepared solution was further dried at room temperature for several days. Scheme 1 presents the schematic view of the above-described reaction. Subsequently, the extracted salt was further purified by successive recrystallization that is used for crystal growth. The attained salt was again dissolved in distilled water to make a saturated solution and placed in a constant temperature bath at 35 °C (±0.1 °C). After 28 days, a good quality single crystal was obtained from the mother solution having dimensions 10x9x2 mm^3, which is shown in the inset of Fig. 1.

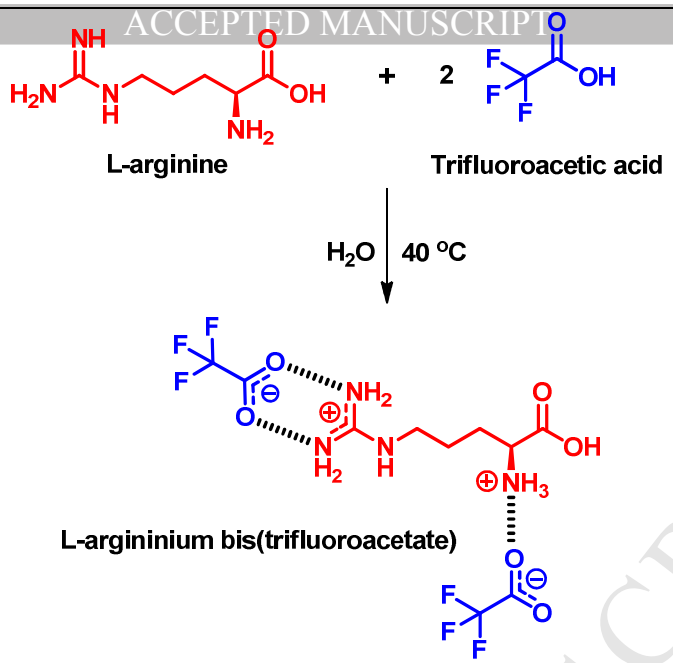

Scheme 1. Synthesis of the titled salt; L-argininium bis(trifluoroacetate).

3. Characterization techniques

3.1. Single crystal X-Ray Diffraction Analysis

Single crystal X-ray diffraction is an analytical and non-destructive technique in which X-rays are subjected to the crystalline material to determine the structure of compounds. A good quality single crystal of dimensions 0.25 × 0.3 × 0.28 mm^3 was selected for above said analysis. Using X'Calibur single crystal diffractometer with MoK_α radiation (λ=0.71069 Å), the diffraction intensities were recorded at 293 K. This analysis reveals that the titled compound crystallizes in $P2_1$ monoclinic crystal system having unit cell dimensions: a = 9.8505 Å, b = 5.7669 Å, c = 14.5035 Å, β = 95.23°.The space group reveals that LABTF single crystal is noncentrosymmetric which is the primary condition for second harmonic generation behavior. These parameters are found to be in a good agreement with the reported literature [22] and confirm the formation of L-arginine bis(trifluoroacetate) crystal.,

An ORTEPIII outlook of the protonated L-argininium cation and trifluoroacetate mono-anions of the titled crystal is presented at the 50 % probability level. Here, hydrogen atoms are demonstrated as capped sticks for clarity (see Fig. 1). The asymmetric entity of the titled crystal contains one molecule of the cationic form of L-arginine (L-argininium) and two mono-anions (I & II) of trifluoroacetic acid (trifluoroacetate). Each of the two trifluoroacetic acid molecules transfers its proton to amino and guanidyl groups of L-arginine molecule forming a doubly charged L-argininium cation. In the trifluoroacetate anions, the larger bond

lengths in the carboxylate groups (C8–O3 = 1.232(5) Å, C8–O4 = 1.238(5) Å, C10–O5 = 1.247(5) Å, & C10–O6 = 1.236(5) Å) provides the information that the hydrogen atom of neutral trifluoroacetic acid gets transformed to the L-arginine molecule. In the intermediate neighborhood of L-argininium cation, it is connected to six trifluoroacetate mono-anions and two L-argininium cations via N-H···O and C-H···O hydrogen bonds (Fig. S1 in supplementary file).

The crystal structure of the three-dimensional network shown in capped stick (L-argininium cation) and space filling (trifluoroacetate anions) views of LABTF unit cell is illustrated in Fig. S2.

In present LABTF crystal structure, L-argininium cations display a supramolecular pattern (See Fig. 2). In the supramolecular chain of L-argininium cations, the amino (–CH–NH3) and carboxylic acid (–COOH) groups are occupied in short N1–H1b•••O1 hydrogen bonds with two neighboring cations. The other O atom (O2) is saturated by a hydrogen bond acceptor [de-protonated trifluoroacetate mono-anion] through O2–H2•••O5 hydrogen bond (see Fig. S1). The other hydrogen bonds of amino and guanidyl groups are linked to other trifluoroacetate mono-anions through strong N–H•••O hydrogen bonds (namely, N4–H4b•••O6, N4–H4a•••O6, N2–H2a•••O3, N1–H1c•••O4 and N1–H1a•••O3). This assembly of L-argininium cations and trifluoroacetate mono-anions leads to an infinite supramolecular chain running parallel to 'b' crystallographic axis. In order to have a 3D insight into the crystal structure of the titled crystal, the auto stereographic projection was drawn. Fig. 3 presents the auto stereogram view of the crystal structure of L-argininium bis(trifluoroacetate) viewed along [010] crystallographic direction.

3.2. Analysis of the Hirshfeld surfaces

Three dimensional molecular Hirshfeld (HF) surfaces mapped over d_{norm} were drawn to have a graphical visual insight of the intermolecular interactions present in the titled crystal system [25,26]. Two contact distances can be associated with each point on the molecular HF surface: one is de indicating the contact distance of the adjacent atom outside from the HF surface and another one is di indicating the contact distance from the point to the adjacent atom inside the HF surface. The d_{norm}; normalized contact distance is a function of both d_e and d_i [27]. The HF surface mapped over d_{norm} wraps both the acceptor as well as the donor interactions on the same surface [28,29]. These HF surfaces are drawn using color code information, which helps in the easy diagnosis of all kinds of intermolecular contacts available in the crystal structure [25,30]. The bright red color spots, white color regions, and

color region on the HF surface represent the overall strongest, weaker and overall weakest contacts. Since the LABTF crystal consists of three individual moieties, we have evaluated the HF surface for all the three (protonated L-argininium cation and two trifluoroacetate mono-anions) moieties individually.

Fig. 4 presents the front and back views of the 3D molecular HF surface plotted over d_{norm} for the L-argininium cation of the titled crystal along with intermolecular contacts (shown using black dashes) with the neighboring L-argininium cations and trifluoroacetate mono-anions. In total, there are nine bright red color circular spots on the HF (d_{norm}) surface visible near hydrogen atoms H1a, H1b, H1c, H2, H2a, H3c, H3d, H4a, and H4b represent the donors of the dominating N-H···O and O-H···O hydrogen bonds, respectively. The other dark red spot near O1 atom represents the acceptor atom for the dominating O1···H1b-N1 hydrogen bond. The other two faint red circular depressions appearing near H3a and H2a hydrogen atoms in Fig. 4 are due to the presence of comparably weak N2-H2a···F1 and C3-H3a···F3 contacts.

The asymmetric unit of the titled crystal contains two molecules of the mono-anionic form of trifluoroacetic acid (trifluoroacetate I & II; see Fig. 1). The crystallographic environment around each of the two mono-anions is different. Thus, the molecular HF surfaces were plotted over d_{norm} for both of these mono-anions of the titled crystal along with neighboring environment mediated by strong hydrogen bonds. Fig. S3 illustrates the front and rear views of the HF surface of trifluoroacetate (I) mono-anion. The four bright red color circular depressions on the d_{norm} surface visible near O3 & O4 present the acceptor atoms of the dominating N-H···O hydrogen bonds, namely N3-H3c···O3, N2-H2a···O3, N1-H1a···O3, & N1-H1c···O4. The other two faint red spots appearing near F1 & F2 in Fig. S3 present the acceptor atoms of the N2-H2a···F1 & C2-H2b···F2 hydrogen bonds, respectively. Similarly, Fig. S4 illustrates the front and back views of the HF surface of trifluoroacetate (II) mono-anion. The dark red color circular depressions on the d_{norm} surface visible near O5 and O6 represent the acceptors of the dominating O-H···O (O2-H2···O5) and N-H···O (N4-H4a···O6, N4-H4b···O6, & N3-H3d···O5) hydrogen bonds.

3.3. Fingerprint analysis

The (2D) fingerprint plot of de against di exemplifies all the intermolecular contacts in the crystal system [29-31]. The overall 2D fingerprint plots along with 3D d_{norm} HF surfaces for the three moieties and those disintegrated into five most significant interactions are displayed in Table 1, 2 and 3. The comparative proportions of various intermolecular

interactions to the overall HF surfaces of trifluoroacetate (I & II) mono-anions and L-argininium cation are represented using a bar chart given in Fig. 5.

For all the three moieties, the O···H/H···O interactions have the most significant contribution (40.7 % in L-argininium cation, 33.4 % in trifluoroacetate (I) mono-anion and 33.6 % in trifluoroacetate (II) mono-anion) to the total HF surface. The sharp spike appearing at $d_i + d_e \sim 1.6$ Å in the 2-D fingerprint plot represents H···O interaction (see row 2 of Table 1), which is attributed to a large number of hydrogen atoms present in the L-argininium cation. Due to a higher number of oxygen atoms in the configuration of trifluoroacetate (I & II) mono-anions there occurs a large spike appearing at $d_i + d_e \sim 1.9$ Å and at $d_i + d_e \sim 1.6$ Å, which represents O···H interaction (see row 3 of Table 2 and row 2 of Table 3). The O···H/H···O interaction give rise to short inter-atomic hydrogen bonds namely, N-H···O, O-H···O and C-H···O bonds. The F···H/H···F interaction is also the most dominant interaction for all the three moieties (29.1 % in L-argininium cation, 36.1 % in trifluoroacetate (I) mono-anion and 32.6 % in trifluoroacetate (II) mono-anion) to their respective HF surfaces. These significant contributions (29.1 %) from H···F contacts to the HF surface indicate the presence of influential C-H···F, N-H···F and O-H···F interactions in the cation. However, for both trifluoroacetate (I & II) moieties, the contribution from F···H contacts (36.1 % & 32.6 %) to the HF surface indicate the presence of acceptor atoms of influential C-H···F, N-H···F and O-H···F interactions in the mono-anions. The involvement of H···H contacts to the HF surface of mono-anions (0.0 %) and cation (17.6 %) clearly explains the hydrogen deficiency and richness in mono-anions and cation, respectively. Similarly, the F···F contacts contribution to the HF surface of mono-anions (I: 14.2 % and II: 11.8 %) and cation (0.0 %) clearly explains the fluorine richness and deficiency in mono-anions and cation, respectively. The bottom right area (see row 6 of Table 1) shows N···H (1.3 %) interactions and top left area represents H···N (1.0 %) interactions for L-argininium moiety. The small contributions (2.0 % in L-argininium cation, 1.0 % in trifluoroacetate (I) mono-anion and 0.8 % in trifluoroacetate (II) mono-anion) from C···H/H···C contacts to the HF surface indicate the absence of C-H···π interactions in the studied crystal structure. For trifluoroacetate mono-anions, O···F/F···O contacts strongly contribute to the HF surface (I: 10.6% & II: 14.8 %). However, for L-argininium moiety, there is comparatively less contribution (3.4 %) from O···F contacts to the HF surface. The 2D fingerprint plots disintegrated into C···C contacts indicate that these interactions have exactly the same involvements (0.2 %) to the overall HF surfaces of cation and mono-anions (see Fig. 5). A small contribution of C···C contacts indicates the absence of π-π stacking in the titled crystal structure.

In all the three moieties, the interatomic C···H/H···C, O···C/C···O, N···F/F···N, O···O, O···N/N···O, C···F/F··C and N···C/C···N contacts contribute very little to the total HF surfaces. Beside these tiny contributions, these contacts play a very major role in crystal packing.

3.4 Crystalline perfection

A good quality single crystal of titled compound was subjected to PANalytical X'Pert PRO MRD High-Resolution X-Ray Diffraction (HRXRD) having $CuK\alpha_1$ radiation source. This technique can be utilized to examine the crystalline perfection of the sample. The diffracting curve (DC) of the specimen has been recorded on the natural facet along a particular direction using ω scan [32]. The monochromated X-ray source beam has been achieved using High-resolution four-bounce Ge (220) monochromator that was further incident on the specimen. A scintillator detector was used to detect the beam diffracted by the sample. The DC recorded for LABTF single crystal for the plane (001) is shown in Fig. 6. The curve contains a single sharp peak having a full width at half maxima (FWHM) of 30 arc sec. The single peak reveals that the titled compound does not contain any structural grain boundaries that show crystalline perfection is quiet good. Since, grain boundaries tend to induce deformities, absence of these in the grown crystal shows its suitability for practical application [33,34]. Moreover, on detailed analysis of diffracting curve it can be seen that the DC is asymmetric with respect to Bragg's peak position. The diffracted intensity found to be slightly higher in a positive direction. This shift towards higher Bragg's angle indicates a decrease in the interplanar distance (d) according to the Bragg's equation. Further, a decrease in 'd' values suggest that the titled compound contains the interstitial point defects. These defects result in compressive stress in the crystal lattice [35,36].

3.5 UV-vis spectral analysis

Optical absorption and cut off wavelength are the important factors for choosing a material in NLO application. Fig. 7 displays the UV-vis absorbance spectra of the L-arginine, Trifluoroacetic acid (TFA) and LABTF compounds (liquid form) in the wavelength range 200 - 1100 nm using SHIMADZU UV-Vis spectrophotometer (Model-1601). The cut-off in the UV-vis region was observed nearly at 226 nm, 213 nm and 239 nm for L-arginine, Trifluoroacetic acid (TAF) and LABTF compounds respectively. Absorption in L-arginine and LABTF was found in the near-ultraviolet region. This is due to charge transfer phenomenon between deprotonated carboxylic and protonated guanidyl groups which results in electronic transistions [23]. It can be concluded that cut-off wavelength in LABTF is

slightly shifted towards the higher wavelength region. This shift is due to change in the molecular interactions between the molecules of L-arginine and TFA compounds.

3.6 Photoluminescence (PL)

Photoluminescence spectroscopy is contactless, non-destructive technique that is utilized to figure out the imperfection or defects present within the host material. In this technique, LABTF single crystal was exposed to high energy photons that results in excitation of its valence electrons from the ground state to excited state and emission spectra were recorded. The complete analyses has been performed using an Edinburgh luminescence spectrometer (Model: F900) fitted with a microsecond xenon flash lamp as a source of excitation at room temperature (~25 ^{o}C). Fig. 8 corresponds to the PL excitation and emission spectra of the titled compound. The emission curve at $??_{Ex}$ = 250nm reveals that the material is suitable for blue light emission as peak maxima were observed at 466 nm which lie in the visible region of the electromagnetic spectrum. There is an additional peak at 558 nm which may be attributed to defects present within the single crystal which was also confirmed through HRXRD analysis.

3.7 Birefringence and laser Shadowgraph

Birefringence interferometry is a sensitive optical technique by which one can measure the birefringence value of a crystal along a particular direction. It will provide significant information about the birefringence inhomogeneities throughout the crystal plate that arises due to inclusions, dislocations, stress or cracks inside the crystal. The optical homogeneity of a flat and well-polished LABTF single crystal of dimensions 10×7×0.5 mm^3 was determined using this technique. The principle and optical schematic of the birefringence interferometry has been described by Verma et al., [37]. Its usage for assessing the birefringence homogeneity of the crystal is reported elsewhere [38]. The interference fringes are shown in Fig. S5 are not of good contrast and also appear to be non-uniform in spacing as well as irregular in shape indicating that the birefringence is not uniform across the sample cross-section. Laser shadowgraph technique was used to observe optical inhomogeneities in the sample [37]. A collimated laser beam was passed through the sample and the image showed local refractive index imperfections in the crystal sample. The dark line in the top of the image shown in Fig. S6 is due to a fine crack in the sample plate. The broad dark regions observed at the right side bottom of the crystal are due to the bending of the laser beam away

by crystal surface which is not normal to the incident beam. The image shows that the crystal has less optical inhomogeneities.

3.8 Photoacoustic spectroscopy

Photoacoustic spectroscopy is a non-destructive tool to measure the absorption coefficient and thermal transport properties of opaque, transparent and diffuse materials in solid, liquid or gas phase which is difficult of measure by other conventional spectroscopic techniques. Photoacoustic spectroscopy works in the principle of conversion of light energy into sound energy. When electromagnetic waves interact with mater, the materials are heated up by the non-radiative transition and this heat will be exchanged to the nearby medium. If the incident light is modulated in acoustic frequencies, there will be a temperature fluctuation in the medium followed by pressure fluctuation. A microphone can be used to detect this pressure wave which carries the signature of thermo-physical properties of the material. An indigenously developed photoacoustic spectrometer is used for the present work. A detail of the experimental setup is being published elsewhere. Briefly, well-collimated light from a 250 W halogen light source is modulated by a two blade chopper and made to focus on the surface of the sample which is placed in an acoustic free photoacoustic cell. A pressure sensor is placed very close to the sample and the signal is recorded digitally using sound recording software. The calibration of the constructed spectrophotometer is performed using the standard samples such as KDP crystal, BK7 glass, and Quartz window. The PA signal for different chopping frequencies and variation of PA signals with the square root of chopping frequency are shown in Fig. 9 and S7 respectively. The thermal diffusivity is derived from the data by curve fitting method [39]. Thermal conductivity and thermal effusivity are calculated from the following relations:

$$k = \alpha \rho cp \qquad (1)$$

$$e = \rho\, cp\sqrt{\alpha} \qquad (2)$$

Where, k, α, ρ, cp and e are the thermal conductivity, thermal diffusivity, density, specific heat capacity, and thermal effusivity of the crystal respectively. From Table 4, it is clear that the thermal parameters of LABTF crystals are higher than standard KDP. Since heat transport properties are crucial in high power laser devices, the knowledge of such values is essential in order to save the devices from thermal damage due to sudden heat exchange. Since the thermo- physical properties of LABTF are higher, it can be used in high power laser devices such as harmonic generators.

3.9 Piezoelectric coefficient

For the measurement of the piezoelectric coefficient, a good quality single crystal having area of 32 mm^2 and thickness of 3.0 mm has been chosen. The opposite surfaces of the sample have been coated with silver paste to make electrodes. Further, the sample was dried on the hot plate at 40ºC for 3 hours in order to make fine coating over it. Piezoelectric response of the organic crystal depends on the packing arrangement of hydrogen bonds and $\pi\cdots\pi$ stacking [40]. The further piezoelectric measurement was conducted using a PM-200 piezometer system to measure d_{22} coefficient of the grown LABTF single crystal at room temperature. The crystal was subjected to a dynamic force of 0.25 N with a frequency of 110 Hz and the obtained value of the piezoelectric coefficient is found to be 1.8 pC/ N. Moreover as a result of promising piezoelectric response on the LABTF single crystal makes leading targets in the application such as electromechanical and energy harvesting devices.

3.10 Shock damage threshold

A sudden release of energy in any form such as mechanical and thermal within a few microseconds results in an instantaneous increase of pressure and temperature. This pulse of energy may be generated by dropping down the crystal or hitting an object on the crystal. Such accidental events can be performed in the laboratory by means of loading shock waves on the crystals with predetermined shock strength to check the ability of the crystal to withstand such events. This experiment has potential applications in the fields of engineering, manufacturing, medical, agriculture, biological and scientific research [41,42]. Shock wave exposure on single crystals induces elastic compression, plastic deformation, structural and phase transformation, transparency changes, refractive index changes, resistivity changes etc. that are reported in literature [43-50]. In the present work, the minimum strength of the shock waves to damage the crystal surface is analyzed. To perform this experiment an indigenously developed hand driven shock tube is used. A well-polished LABTF crystal shown in Fig. S8(a) of thickness 2mm is placed at a distance of 1 cm from the open end of the driven section for exposing the shock waves. Initially, the crystal is loaded with Mach number 1 and subsequently the strength is increased up to Mach number 2.4 (Mach number is a measure of the strength of shock waves). After every shock, the surface of the crystal is analyzed by an optical microscope to investigate the changes induced by the shock waves. It is noticed that there are no changes for the shock pulses of Mach number 1, 1.2, 1.3, 1.7, 2.0, 2.2 and 2.3. However, when the Mach number is increased to 2.4, the surface of the crystal started to damage and a number of tiny crystals appear on the surface as seen in the Fig. S8(b). It is

interesting to notice that when shock waves are applied to the crystal, it peels off the crystallites but not breaking the crystal. Finally, for the 15th shock, the crystal got crack as shown in the Fig. S8(c).

3.11 Nanoindentation

Whenever a material is used in industrial applications, it is susceptible to various kinds of damages during handling, consolidation etc. Apart from these, NLO Crystals are used in laser applications, therefore, these crystals may suffer damage due to high laser intensity when used above its threshold limit. For a stable device, a crystal with high LDT value has been desirable. A high laser damage is somewhat dependent on material's mechanical stability like hardness, stiffness and Young's modulus etc. In order to investigate the above-mentioned parameters at the nanoscale, nanoindentation technique was employed on titled compound [51]. The nanoindentation measurement was accomplished using a three-sided pyramidal Berkovich diamond indenter having nominal edge radius of 20 nm. The diamond indentor is affixed to a calibrated nanoindentor (TTX-NHT, CSM Instruments) and its faces are at 65.3° from the vertical axis. The material was tested under progressive multicycle loading with an acquisition rate of 10 Hz. The approach speed was maintained at 2000 nm/min with a load range of 5 to 150 mN. The loading-unloading speed was set at 20mN/min with dwell period of 10 seconds and pause time of 10 seconds in between each cycle. In addition, high-resolution Atomic Force Microscope (AFM) technique was utilized to obtain the topographic image of the indented surface. These images facilitated the visualization of deformations or cracks caused due to the applied load. For this analysis, standard Oliver and Pharr method [52] was scrutinized. Using the following relation, a loading-unloading curve can be plotted

$$F = \alpha(h - h_f)^m \qquad (3)$$

Where F is the load applied to the specimen, α and m is the experimental parameters, h_f is the final displacement after completing the loading and unloading curve. The stiffness of the sample was approximated from the obtained unloading curve,

$$s = \frac{dF}{dh} = \alpha m(h - h_f)^{m-1} \qquad (4)$$

Further, the contact depth was evaluated using the above-obtained stiffness value and following mentioned relation,

$$h_c = h_{max} - \varepsilon \times \frac{F_{max}}{S} \qquad (5)$$

Where ε is equal to 0.75 which is an indenter constant, h_{max} is the maximum displacement of the indenter in the crystal with load and h_c is the contact depth. The hardness of the material can be calculated using the determined contact depth from the relation,

$$H = \frac{F_{max}}{A} \qquad (6)$$

Where H is the hardness of the material, F_{max} is the maximum indenter load applied to the material and A is the area of contact of indentor. The load independent hardness is denoted as H_o, which can be calculated by empirical relation.

$$H_0 = Ka_2 \qquad (7)$$

Where the constant K is a geometry-dependent quantity of indenter having the value 1/24.5, a_2 is a constant which can be estimated by fitting the polynomial curve between peak load and contact depth curve. Further, Young's modulus can be evaluated from the unloading curve by the formula

$$E = \frac{1\sqrt{\pi}}{2A}\frac{dF}{dh} \qquad (8)$$

In the present study, a well-polished surface of the titled compound was subjected to this measurement. Using AFM in contact mode, the RMS roughness parameter of 113 nm was obtained as shown in Fig. S9. The loading and unloading curves are shown in Fig. 10 were obtained from the previously described procedure for (001) plane of LABTF single crystal., For the close assessment of these curves, an expanded view is shown in Fig. S10 at individual loads. The traces of slight pop-in were observed in the load range from 5mN to 75mN. This pop-in occurs when there is a transformation from elastic to the elastic/plastic region. This transformation arises due to nucleation of plastic deformations owing to defects for instance dislocations, point defects and cracks within the single crystal [15]. The pop-in's concentration found to be increasing as we further increase the applied. The vigorous visibility of pop-in can be observed at 150 mN that reveals the occurrence of cracks in the crystal. The formation of cracks within the single crystal after load application can be visualized via comparing optical images obtained before and after experiment as shown in Fig. S11 (a,b). The cross-section profile of the depth after indentation with 30mN load and the AFM imprint made by the same load is shown in the Fig. S12. The obtained depth profile from nanoindentation is found to be the in good correlation with the AFM profile.

Further, various parameters corresponding to the mechanical characteristics were computed from the analysis of obtained load-displacement curves and listed in Table 5. Fig. S13 represents the curve between Contact depth and the d peak load. The contact depth tends to

increase with an increase in peak load. This curve was fitted with polynomial function and the values of constants a_0, a_1 and a_2 were obtained using the relation

$$F_{max} = a_0 + a_1 h_c + a_2 {h_c}^2 \qquad (9)$$

The obtained value of the a_2 coefficient is 6.149X10^{-6} mN nm^{-2}. Using the equation $H_0 = ka_2$ the value of load independent hardness was found to be 0.250 GPa or 250 MPa. The obtained hardness value found to be higher than L-Prolinium Tartrate (131 MPa) [53] and lesser than L-Arginine 4-nitrophenolate 4-nitrophenol dihydrate (450MPa) [17], L - Threoninium picrate (352.68 MPa) [54]. These results show that the crystal has moderate mechanical strength to resist deformation. The P-h curve assist in evaluation of young's modulus. The extracted values of young's modulus were plotted with peak load as shown in Fig. S14. From the curve, it has been observed that the value of young's modulus decreases with increase in peak load which may be due to tip rounding of indenter. Fig. S15 shows the variation of initial loading stiffness with the contact depth at peak load. Further, the relation between initial loading stiffness (S), contact depth (h_c), reduced young's modulus and constant 'a' that is related to indentation tip rounding is given as

$$S = a + bh_c \qquad (10)$$

A linear function is fitted to the curve. The slope of the fitted curve (b) represents the reduced young's modulus. In the present case, the slope was found to be 5.01X10^{-5} mN nm^{-2}. The reduced Young's modulus was estimated to be 50.1 GPa for the indentation made on LABTF single crystal. Hence, these studies on LABTF single crystal signifies that it possess reasonable mechanical properties.

4. **Conclusion**

A single crystal of LABTF has been grown using Slow evaporation solution growth technique after making many trail experiments. Single crystal XRD analysis of titled compound showed that it crystallized in monoclinic crystal system and lattice dimensions in good agreement with reported one. The asymmetric unit of the obtained crystal consists of one L-argininium cation and two trifluoroacetate mono-anions. 3D Hirshfeld surface and 2D fingerprint plot studies envisaged all the non-covalent contacts present in the LABTF crystal system. Indeed, O···H/H···O contacts possess the largest involvement in the overall molecular Hirshfeld surface of all the three moieties. HRXRD studies revealed that the specimen is free from any structural grain boundaries and contain only a single peak. Thus, the crystalline perfection of a titled compound found to be good. Photoluminescence analysis divulged that

the host material emits in the blue region of visible light. The optical behavior of the single crystal was characterized by birefringence and it was found to be non-uniform across the sample cross-section. Shock damage threshold analysis revealed that the specimen withstand the shock wave up to Mach no. 2.3. However, when the Mach number is increased to 2.4, the surface of the crystal started damage or crack appeared on the surface. Thermal analysis using photoacoustic technique revealed that crystal possesses reasonably good thermal parameters and can be used for high power laser devices. Mechanical studies showed that LABTF single crystal possesses moderate mechanical stability.

5. Conflicts of interest

There are no conflicts of interest to declare.

6. Acknowledgment

The authors are highly thankful to Director, CSIR- NPL for his continuous support and encouragement in carrying out the present work. One of the authors Sonia would like to thank CSIR for providing SRF fellowship.

References:-

1. D.S. Chemla, J. Zyss, Nonlinear optical properties of organic molecules and crystals Volume 1 Volume 1, Academic Press, Orlando, 1987.
2. V.G. Dmitriev, G.G. Gurzadjan, D.N. Nikogosjan, Handbook of nonlinear optical crystals, 3. rev. ed., softcover reprint of the hardcover 3rd ed. 1999, Springer, Berlin, 2010.
3. M.S. Wong, C. Bosshard, F. Pan, P. Günter, Non-classical donor-acceptor chromophores for second order nonlinear optics, Adv. Mater. 8 (1996) 677–680.
4. R.W. Boyd, Nonlinear optics, 3rd ed, Academic Press, Amsterdam ; Boston, 2008.
5. L.R. Dalton, Organic electro-optics and photonics: molecules, polymers and crystals, University Printing House, Materials Research Society, Cambridge, United Kingdom, 2015.
6. G. Raos, M. Del Zoppo, Substituent effects on the second-order hyperpolarisability of cyanine cations, J. Mol. Struct. THEOCHEM. 589-590 (2002) 439–445.
7. J Jayabharathi, V Thanikachalam, K Jayamoorthy, MV Perumal Spectrochimica Acta Part A: Molecular and Biomolecular Spectroscopy 79 (1), 2011, 6-16.
8. J. Jayabharathi, V. Thanikachalam, V. Kalaiarasi, K. Jayamoorthy, Optical properties of 1-(4,5-diphenyl-1-p-tolyl-1H-imidazol-2-yl)naphthalen-2-ol – ESIPT process, Spectrochimica Acta Part A: Molecular and Biomolecular Spectroscopy. 120 (2014), 389-394.

9. J. Jayabharathi, V. Thanikachalam, K. Jayamoorthy, Photophysical studies of some heterocyclic chromophores as potential NLOmaterials Spectrochimica Acta Part A: Molecular and Biomolecular Spectroscopy. 89 (2012), 301-307.
10. S.R. Marder, J.E. Sohn, G.D. Stucky, American Chemical Society, American Chemical Society, American Chemical Society, eds., Materials for nonlinear optics: chemical perspectives, American Chemical Society, Washington, DC, 1991.
11. P.N. Prasad, D.J. Williams, Introduction to nonlinear optical effects in molecules and polymers, Wiley, New York, 1991.
12. J. Jayabharathi, V. Thanikachalam, K. Jayamoorthy, Physicochemical studies of chemosensor imidazole derivatives:DFT based ESIPT process Spectrochimica Acta Part A: Molecular and Biomolecular Spectroscopy. 89 (2012), 168-176.
13. J. Jayabharathi, V. Thanikachalam, K. Jayamoorthy, M.V. Perumal, Computational studies of 1,2-disubstituted benzimidazole derivatives Spectrochimica Acta Part A: Molecular and Biomolecular Spectroscopy. 97 (2012), 131-136.
14. J. Jayabharathi, V. Thanikachalam, K. Jayamoorthy, Optical properties of 1,2-diaryl benzimidazole derivatives ‐ A combinedexperimental and theoretical studies Spectrochimica Acta Part A: Molecular and Biomolecular Spectroscopy. 115 (2013), 74-78.
15. B.A. Fuchs, C.K. Syn, S.P. Velsko, Diamond turning of L-arginine phosphate, a new organic nonlinear crystal, Appl. Opt. 28 (1989) 4465.
16. A. Delfino, Comprehensive Optical Second Harmonic Generation Study of the Non-Centrosymmetric Character of Biological Structures, Mol. Cryst. Liq. Cryst. 52 (1979) 271–284.
17. Sonia, N. Vijayan, M. Vij, P. Kumar, B. Singh, S. Das, R. Rajnikant, S. H., Assessment of the imperative features of an l -arginine 4-nitrophenolate 4-nitrophenol dihydrate single crystal for non linear optical applications, Mater Chem Front. 1 (2017) 1107–1117.
18. L. Wang, G.H. Zhang, X.T. Liu, L.N. Wang, X.Q. Wang, L.Y. Zhu, D. Xu, A novel l-arginine salt nonlinear optical crystal: l-arginine p-nitrobenzoate monohydrate (LANB), J. Mol. Struct. 1058 (2014) 155–162.
19. T. Pal, T. Kar, G. Bocelli, L. Rigi, Synthesis, Growth, and Characterization of l -Arginine Acetate Crystal: A Potential NLO Material, Cryst. Growth Des. 3 (2003) 13–16.
20. A.. Petrosyan, R.. Sukiasyan, H.. Karapetyan, S.. Terzyan, R. Feigelson, Growth and investigation of new non-linear optical crystals of LAP family, J. Cryst. Growth. 213 (2000) 103–111.

21. L. Xian, S. Liu, Y. Ma, G. Lu, Influence of hydrogen bonds on charge distribution and conformation of l-arginine, Spectrochim. Acta. A. Mol. Biomol. Spectrosc. 67 (2007) 368–371.
22. M.R. Silva, J.A. Paixão, A.M. Beja, L -Argininium bis(trifluoroacetate), Acta Crystallogr. Sect. E Struct. Rep. Online. 59 (2003) o1912–o1914.
23. Z. Sun, G. Zhang, X. Wang, Z. Gao, X. Cheng, S. Zhang, D. Xu, Growth, Morphology, Thermal, Spectral, Linear, and Nonlinear Optical Properties of L -Arginine Bis(trifluoroacetate) Crystal, Cryst. Growth Des. 9 (2009) 3251–3259.
24. A. Katrusiak, Crystallographic autostereograms, J. Mol. Graph. Model. 19 (2001) 363–367. doi:10.1016/S1093-3263(00)00085-1.
25. F.L. Hirshfeld, Bonded-atom fragments for describing molecular charge densities, Theor. Chim. Acta. 44 (1977) 129–138. doi:10.1007/BF00549096.
26. S. Goel, H. Yadav, N. Sinha, B. Singh, I. Bdikin, D.C. Rao, K. Gopalaiah, B. Kumar, An insight into the synthesis, crystal structure, geometrical modelling of crystal morphology, Hirshfeld surface analysis and characterization of *N* -(4-methylbenzyl)benzamide single crystals, J. Appl. Crystallogr. 50 (2017) 1498–1511. doi:10.1107/S1600576717012316.
27. S. Goel, H. Yadav, N. Sinha, B. Singh, I. Bdikin, B. Kumar, X-ray, dielectric, piezoelectric and optical analyses of a new nonlinear optical 8-hydroxyquinolinium hydrogen squarate crystal, Acta Crystallogr. Sect. B Struct. Sci. Cryst. Eng. Mater. 74 (2018) 12–23. doi:10.1107/S2052520617013038.
28. J.J. McKinnon, D. Jayatilaka, M.A. Spackman, Towards quantitative analysis of intermolecular interactions with Hirshfeld surfaces, Chem. Commun. (2007) 3814. doi:10.1039/b704980c.
29. H. Yadav, N. Sinha, S. Goel, B. Singh, I. Bdikin, A. Saini, K. Gopalaiah, B. Kumar, Growth, crystal structure, Hirshfeld surface, optical, piezoelectric, dielectric and mechanical properties of bis(L -asparaginium hydrogensquarate) single crystal, Acta Crystallogr. Sect. B Struct. Sci. Cryst. Eng. Mater. 73 (2017) 347–359. doi:10.1107/S2052520617002906.
30. H. Yadav, N. Sinha, S. Goel, A. Hussain, B. Kumar, Growth and structural and physical properties of diisopropylammonium bromide molecular single crystals, J. Appl. Crystallogr. 49 (2016) 2053–2062. doi:10.1107/S1600576716014552.
31. M.A. Spackman, J.J. McKinnon, Fingerprinting intermolecular interactions in molecular crystals, CrystEngComm. 4 (2002) 378–392. doi:10.1039/B203191B.
32. S.K. Kushwaha, M. Shakir, K.K. Maurya, A.L. Shah, M.A. Wahab, G. Bhagavannarayana, Remarkable enhancement in crystalline perfection, second harmonic generation efficiency,

optical transparency, and laser damage threshold in potassium dihydrogen phosphate crystals by L-threonine doping, J. Appl. Phys. 108 (2010) 033506.

33. B.W. Batterman, H. Cole, Dynamical Diffraction of X Rays by Perfect Crystals, Rev. Mod. Phys. 36 (1964) 681–717. doi:10.1103/RevModPhys.36.681.
34. Sonia, N. Vijayan, M. Bhushan, K. Thukral, R. Raj, K.K. Maurya, D. Haranath, S.A. Martin Britto Dhas, Growth of a bulk-size single crystal of sulphamic acid by an in-house developed seed rotation solution growth technique and its characterization, J. Appl. Crystallogr. 50 (2017) 763–768.
35. G. Bhagavannarayana, S. Parthiban, S. Meenakshisundaram, An Interesting Correlation between Crystalline Perfection and Second Harmonic Generation Efficiency on KCl- and Oxalic Acid-Doped ADP Crystals, Cryst. Growth Des. 8 (2008) 446–451.
36. K. Lal, G. Bhagavannarayana, A high-resolution diffuse X-ray scattering study of defects in dislocation-free silicon crystals grown by the float-zone method and comparison with Czochralski-grown crystals, J. Appl. Crystallogr. 22 (1989) 209–215S. Verma and P.J. Shlichta, *Prog. Cryst. Growth Charact. Mater*., 2008, **54**, 1–120.
37. S. Verma, P.J. Shlichta, Imaging techniques for mapping solution parameters, growth rate, and surface features during the growth of crystals from solution, Prog. Cryst. Growth Charact. Mater. 54 (2008) 1–120.
38. S.K. Sharma, Y. Singh, S. Verma, M.K. Singh, K.S. Bartwal, P.K. Gupta, Growth of L - arginine phosphate monohydrate crystals in different orientations to achieve isometric morphology for device applications, CrystEngComm. 18 (2016) 6403–6410.
39. W.L.B. Melo, R.M. Faria, Photoacoustic procedure for measuring thermal parameters of transparent solids, Appl. Phys. Lett. 67 (1995) 3892–3894.
40. K.A. Werling, G.R. Hutchison, D.S. Lambrecht, Piezoelectric Effects of Applied Electric Fields on Hydrogen-Bond Interactions: First-Principles Electronic Structure Investigation of Weak Electrostatic Interactions. The Journal of Physical Chemistry Letters 4 (2013), 1365–1370.
41. G. Jagadeesh, Industrial applications of shock waves, J. Aero. Engg. 222 (2008) 575- 583
42. G. Jagadeesh, K. Takayama, Novel applications of micro-shock waves in biological sciences, J.Indian Inst. Sci. 82 (2002) 49–57.
43. J. Zhang, P.S. Branicio, Molecular Dynamics Simulations of Plane Shock Loading in SiC, Procedia Eng. 75 (2014) 150–153.
44. V.A. Gnatyuk, T. Aoki, Y. Hatanaka, Laser-induced shock wave stimulated doping of CdTe crystals, Appl. Phys. Lett. 88 (2006) 242111.

45. S.-N. Luo, T.C. Germann, D.L. Tonks, Q. An, Shock wave loading and spallation of copper bicrystals with asymmetric Σ3⟨110⟩ tilt grain boundaries, J. Appl. Phys. 108 (2010) 093526.
46. D.E. Hooks, K.J. Ramos, A.R. Martinez, Elastic-plastic shock wave profiles in oriented single crystals of cyclotrimethylene trinitramine (RDX) at 2.25GPa, J. Appl. Phys. 100 (2006) 024908.
47. F. Müller, E. Schulte, Shock Wave Compression of NaCl Single Crystals observed by Flash-X-Ray Diffraction, Z. Für Naturforschung A. 33 (1978).
48. Z.A. Dreger, Y.A. Gruzdkov, Y.M. Gupta, J.J. Dick, Shock Wave Induced Decomposition Chemistry of Pentaerythritol Tetranitrate Single Crystals: Time-Resolved Emission Spectroscopy, J. Phys. Chem. B. 106 (2002) 247–256.
49. P.A. Urtiew, Effect of shock loading on transparency of sapphire crystals, J. Appl. Phys. 45 (1974) 3490–3493.
50. S.T. Weir, A.C. Mitchell, W.J. Nellis, Electrical resistivity of single-crystal Al_2O_3 shock-compressed in the pressure range 91–220 GPa (0.91–2.20 Mbar), J. Appl. Phys. 80 (1996) 1522–1525.
51. I. Bdikin, B. Singh, J. Suresh Kumar, M.P.F. Graça, A.M. Balbashov, J. Grácio, A.L. Kholkin, Nanoindentation induced piezoelectricity in SrTiO3 single crystals, Scr. Mater. 74 (2014) 76–79.
52. W.C. Oliver, G.M. Pharr, An improved technique for determining hardness and elastic modulus using load and displacement sensing indentation experiments, J. Mater. Res. 7 (1992) 1564–1583.
53. K. Thukral, N. Vijayan, B. Singh, I. Bdikin, D. Haranath, K.K. Maurya, J. Philip, H. Soumya, P. Sreekanth, G. Bhagavannarayana, Growth, structural and mechanical analysis of a single crystal of L -prolinium tartrate: a promising material for nonlinear optical applications, CrystEngComm. 16 (2014) 9245–9254.
54. A. Krishna, N. Vijayan, S. Gupta, K. Thukral, V. Jayaramakrishnan, B. Singh, J. Philip, S. Das, K.K. Maurya, G. Bhagavannarayana, Key aspects of L -threoninium picrate single crystal: an excellent organic nonlinear optical material with a high laser-induced damage threshold, RSC Adv. 4 (2014) 56188–56199.

Figure Captions

Fig. 1 The ORTEPIII view of the L-argininium bis(trifluoroacetate) compound with atomic numbering scheme. The non-hydrogen atoms are drawn using 50 % probability thermal ellipsoids. Fluorine, oxygen, Nitrogen and carbon atoms are represented as yellowish-green, red, blue and dark grey colour ellipsoid balls, respectively. For the sake of clear vision, the hydrogen atoms are presented by green colour capped sticks. The inset presents the photograph of as grown LABTF crystal.,

Fig. 2 Autostereographic projection [24] of the crystal structure of L-argininium bis(trifluoroacetate) viewed along 'b' crystallographic direction

Fig. 3 Infinite supramolecular chain of l-argininium cations bonded through N1–H1b•••O1 hydrogen bonds.

Fig. 4 Two views of Molecular Hirshfeld surface plotted over d_{norm} for L-argininium cation connected to intermediate trifluoroacetate and L-argininium moieties via intermolecular hydrogen-bonding interactions.

Fig.5 Relative contributions of different interactions to the Hirshfeld surface area in L-argininium and trifluoroacetate (I & II) moieties of the titled compound.

Fig. 6 Rocking curve recorded for a plane (001) of LABTF Single crystal

Fig. 7 UV-Vis spectrum of L-Arginine, TFA and LABTF compounds

Fig. 8 PL Spectrum for LABTF

Fig. 9 Variation of PA signal Vs. time for different frequencies for LABTFA

Fig. 10 Loading-Unloading curve of LABTF Single crystal

Table captions

Table 1. 2-D fingerprint plots and 3D (d_{norm}) Hirshfeld surfaces typifying five most significant contributions of various molecular interactions for L-argininium moiety.

Table 2. 2-D fingerprint plots and 3D (d_{norm}) Hirshfeld surfaces typifying five most significant contributions of various molecular interactions for trifluoroacetate mono-anion (I).

Table 3. 2-D fingerprint plots and 3D (d_{norm}) Hirshfeld surfaces typifying five most significant contributions of various molecular interactions for trifluoroacetate mono-anion (II).

Table 4 Thermophysical properties of LABTF

Table 5 Various obtained parameters related to mechanical properties of LABTF single crystal along the (001) plane

Table 1

S. No.	Various Interactions	2D Fingerprint Plots	3D (d_{norm}) Hirshfeld Surface (Front)	3D (d_{norm}) Hirshfeld Surface (Back)
1.	All Interactions (100 %)	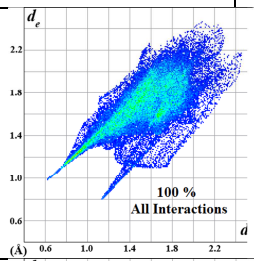	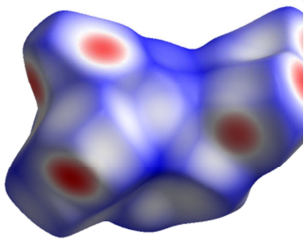	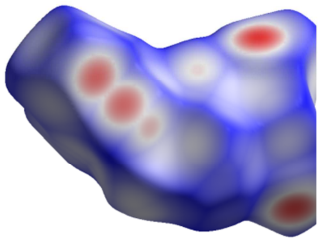
2.	O···H/H···O (40.7 %)	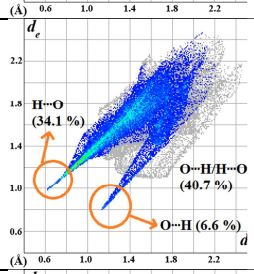	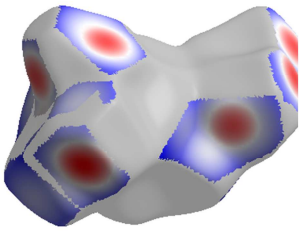	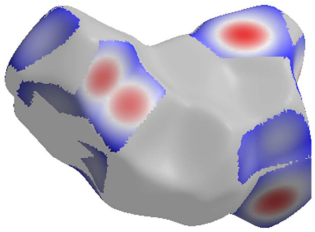
3.	H···F (29.1 %)	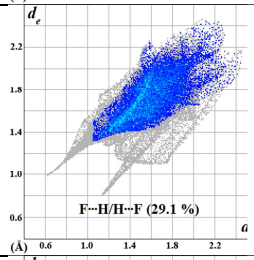	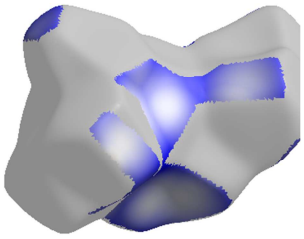	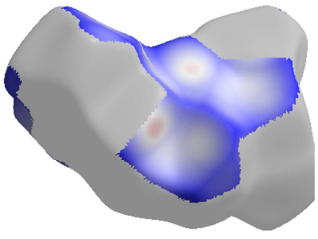
4.	H···H (17.6 %)	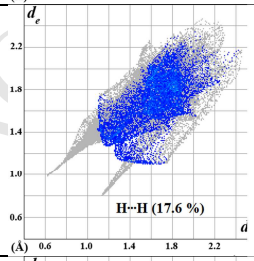	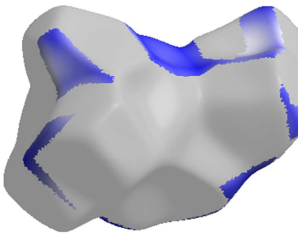	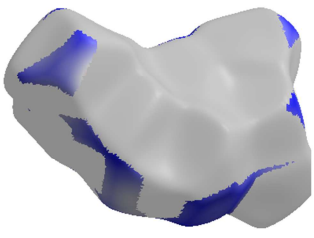
5.	O···F (3.4 %)	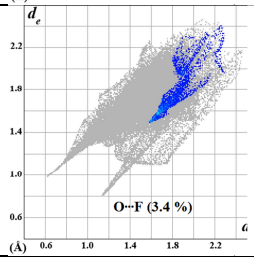	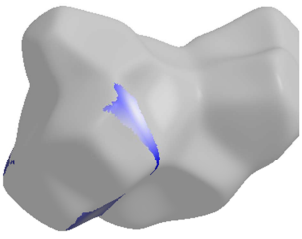	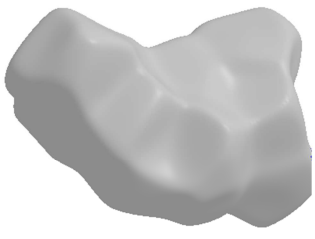

6.	N···H/H···N (2.3 %)	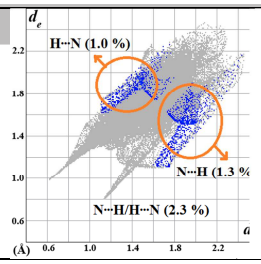	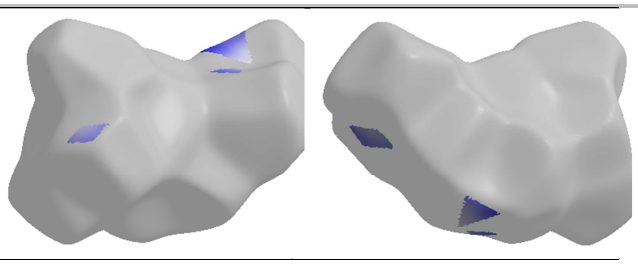

Table 2.

S. No.	Various Interactions	2D Fingerprint Plots	3D (d_{norm}) Hirshfeld Surface (Front)	3D (d_{norm}) Hirshfeld Surface (Back)
1.	All Interactions (100 %)	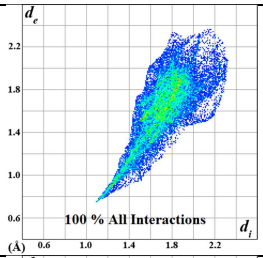	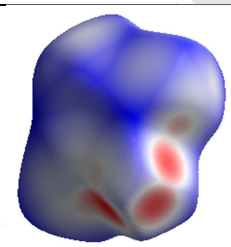	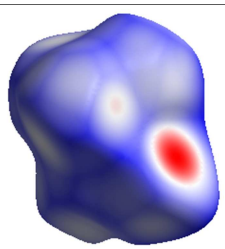
2.	F···H (36.1 %)	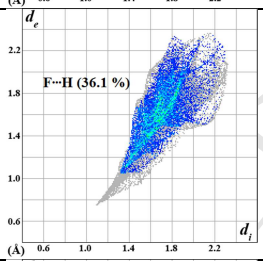	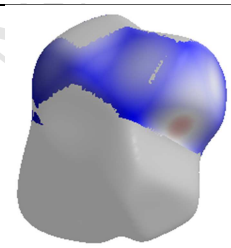	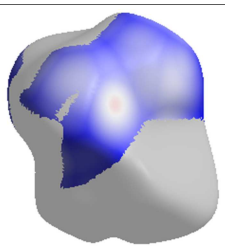
3.	O···H (33.4 %)	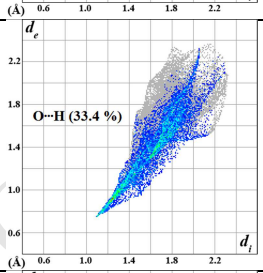	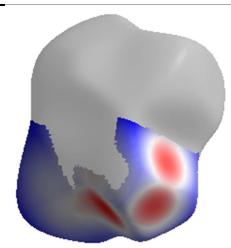	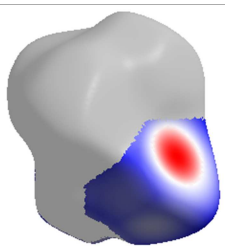
4.	F···F (14.2 %)	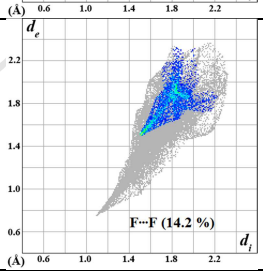	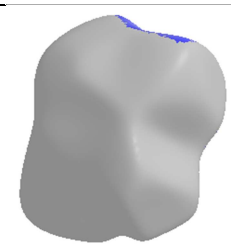	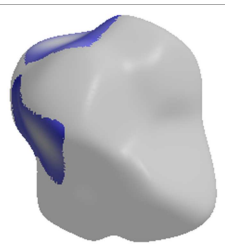

5.	O···F/F···O (10.6 %)	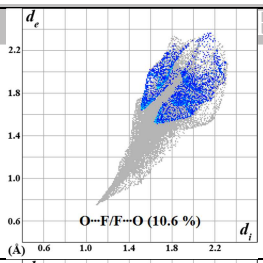	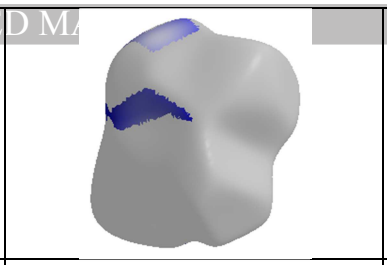	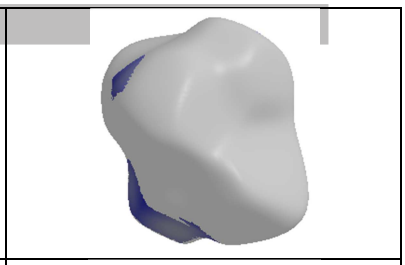
6.	O···C/C···O (2.1 %)	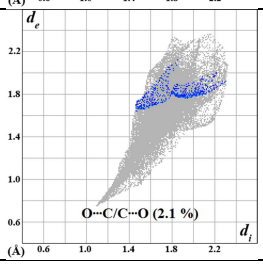	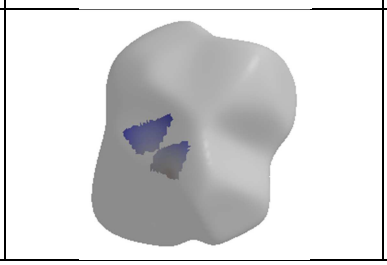	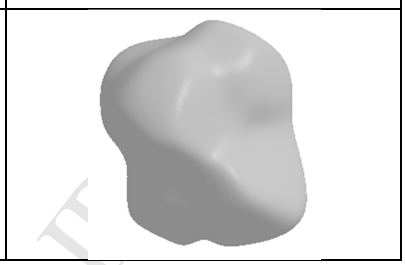

Table 3.

S. No.	Various Interactions	2D Fingerprint Plots	3D (d_{norm}) Hirshfeld Surface (Front)	3D (d_{norm}) Hirshfeld Surface (Back)
1.	All Interactions (100 %)	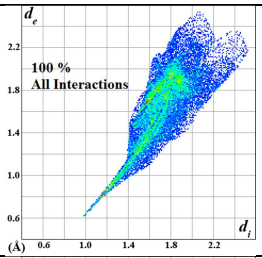	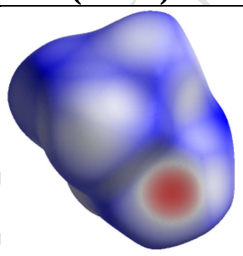	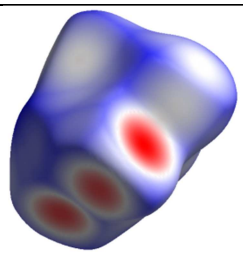
2.	O···H (33.6 %)	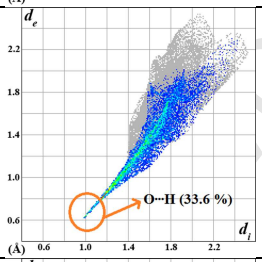	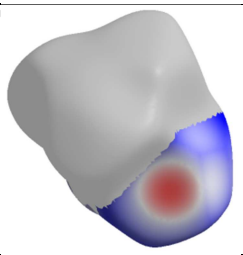	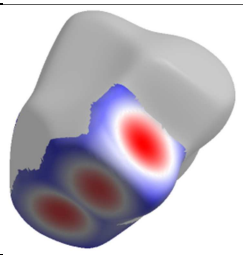
3.	F···H (32.6 %)	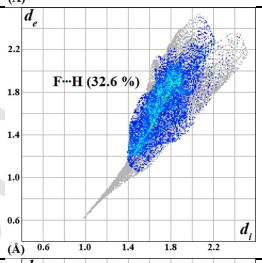	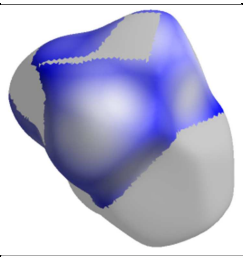	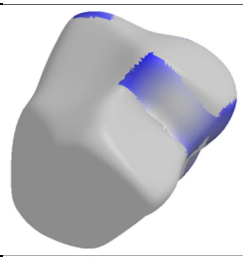
4.	O···F/F···O (14.8 %)	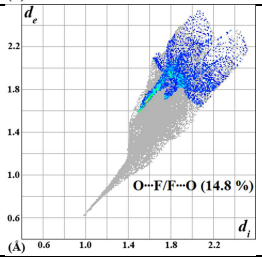	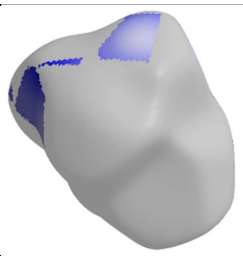	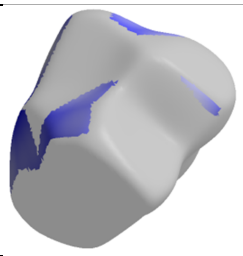

5.	F···F (11.8 %)	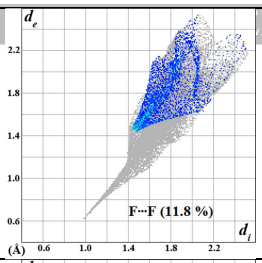	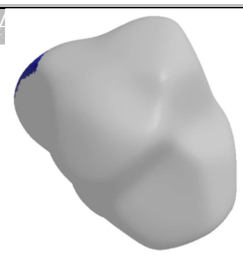	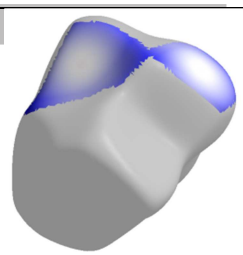
6.	C···F/F···C (2.3 %)	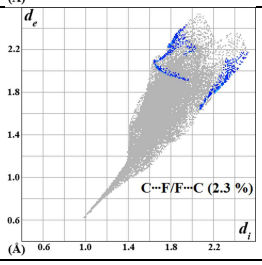	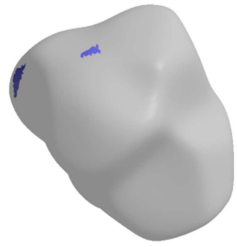	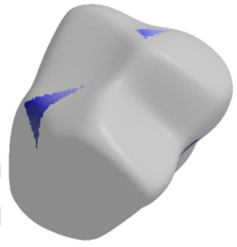

Table 4.

Sample Name	Thermal diffusivity 10^{-6} (m^2/s)	Thermal Effusivity 10^3 ($m^{-2}K^{-1}S^{-1/2}$)	Thermal Conductivity ($Wm^{-1}K^{-1}$)
KDP	0.970	1.974	1.944
LABTFA	1.179	2.830	3.074

Table5.

F (mN)	Hit (MPa)	Eit (GPa)	h_m (nm)	S [mN nm^{-1}]	h_c (nm)	h_r (nm)	h_p (nm)	A_P (nm^{-2})	M
5.04	1156.7	16.987	16.987	0.0447	540.5	512.56	455.38	4359567	1.48
10.05	838.96	15.926	15.926	0.0696	935.06	897.65	799.09	11974702	1.64
20.04	650.97	14.302	14.302	0.1004	1456.62	1406.27	1299	30791074	1.53
30.04	547.02	13.2	13.2	0.1238	1890.21	1827.86	1681.91	54909588	1.6
50.05	448.7	11.522	11.522	0.1543	2594.87	2513.77	2356.37	1.12E+08	1.5
75.06	429.67	11.484	11.484	0.1925	3173.23	3071.75	2816.82	1.75E+08	1.66
100.06	396.81	10.678	10.678	0.2152	3744.7	3624.78	3348.28	2.52E+08	1.62
150.08	368.86	9.7108	9.7108	0.2488	4654.58	4506.63	4247.53	4.07E+08	1.45

Figures

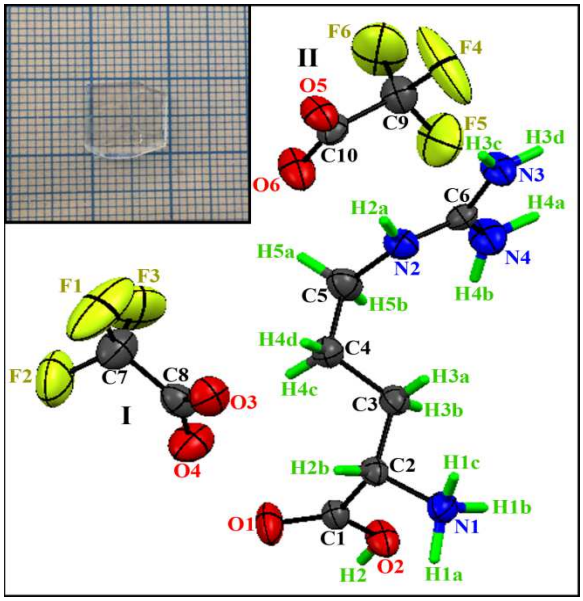

Fig. 1

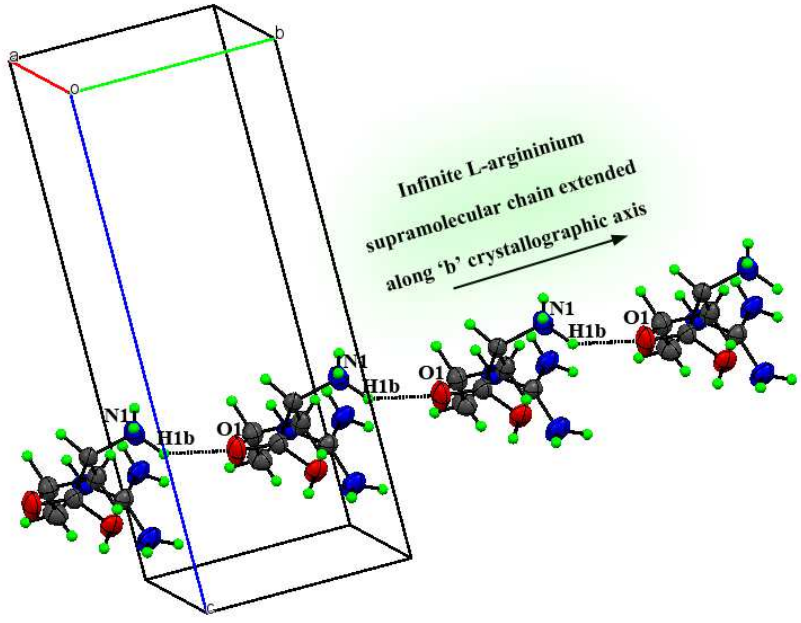

Fig. 2

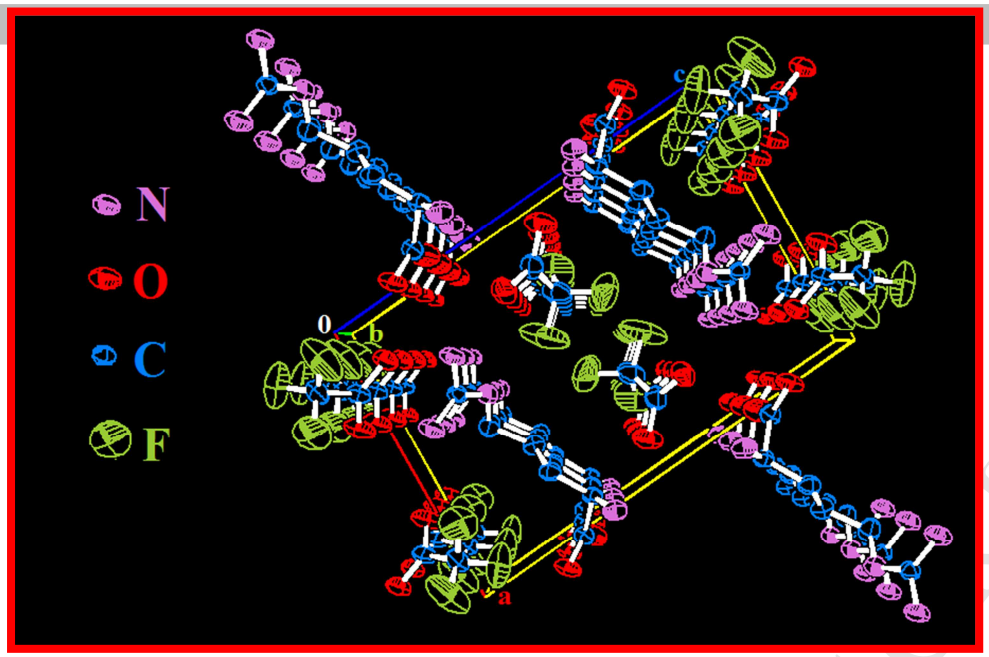

Fig. 3

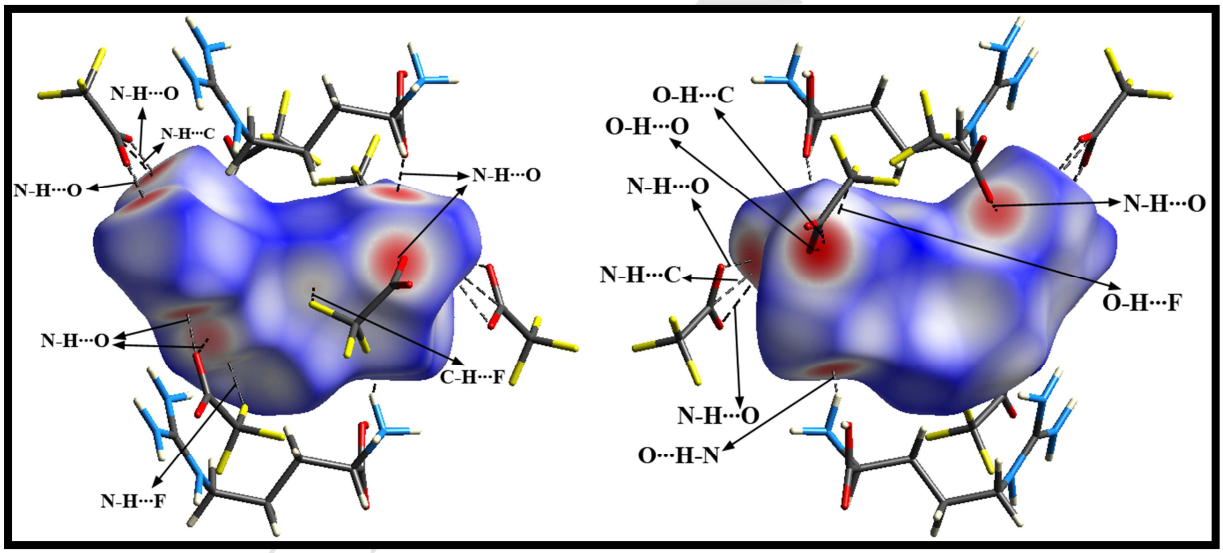

Fig. 4

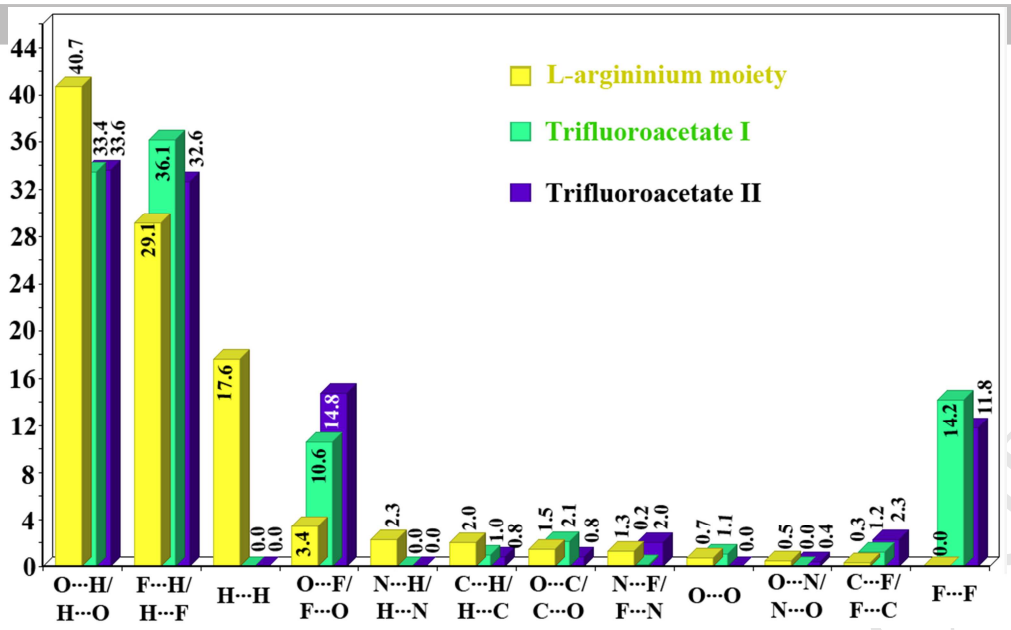

Fig. 5

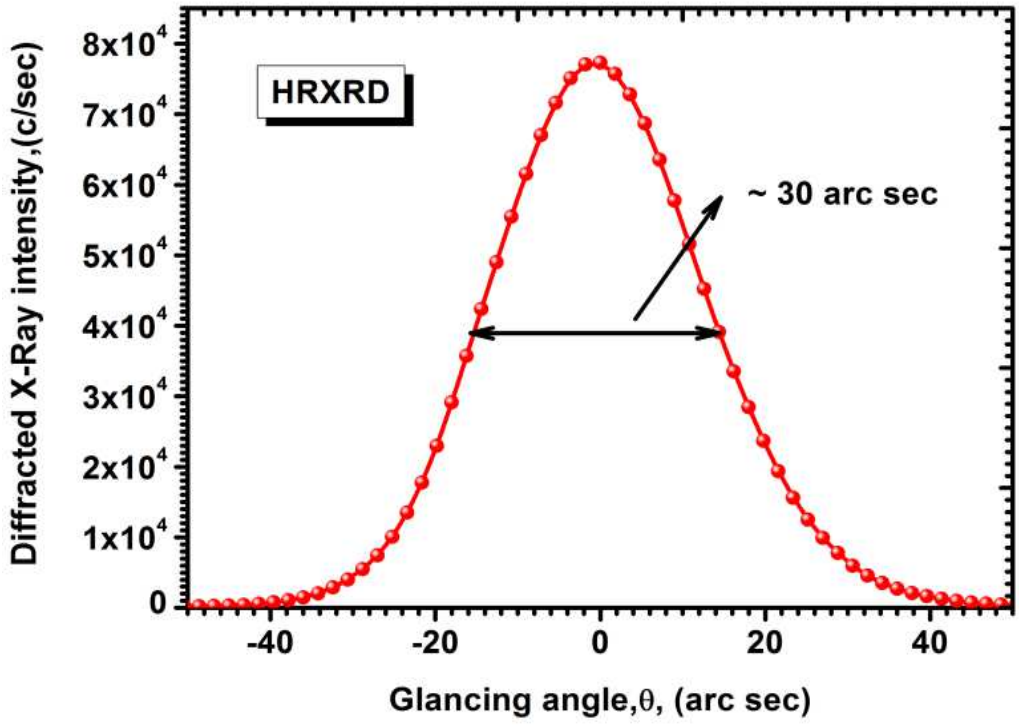

Fig. 6

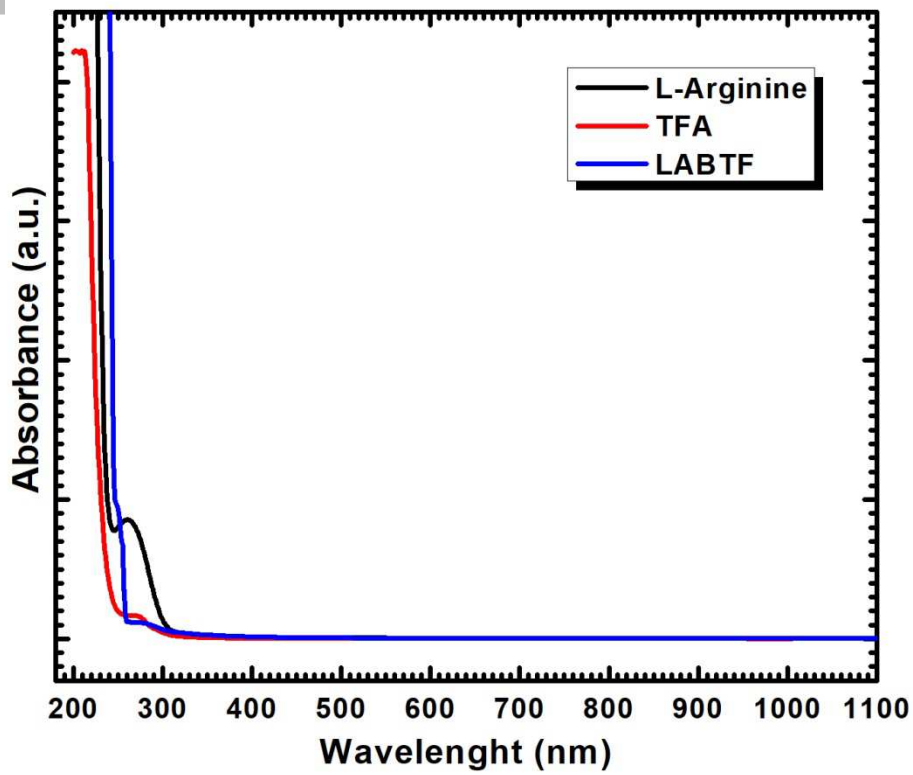
L-Arginine
TFA
LABTF
Absorbance (a.u.)
200 300 400 500 600 700 800 900 1000 1100
Wavelenght (nm)

Fig. 7

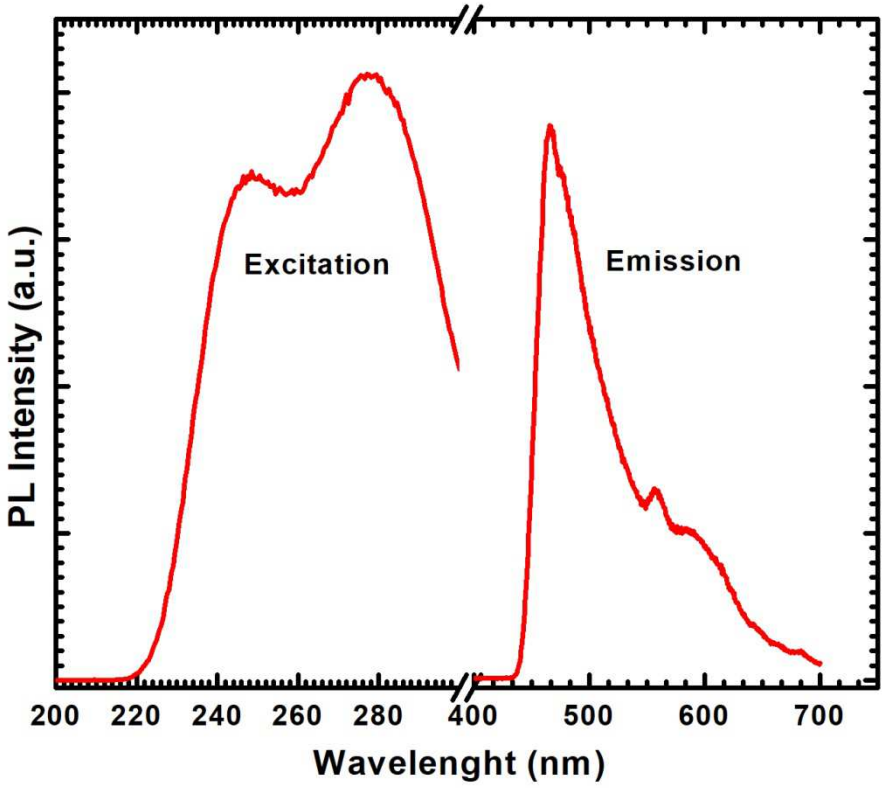
Excitation
Emission
PL Intensity (a.u.)
200 220 240 260 280 400 500 600 700
Wavelenght (nm)

Fig. 8

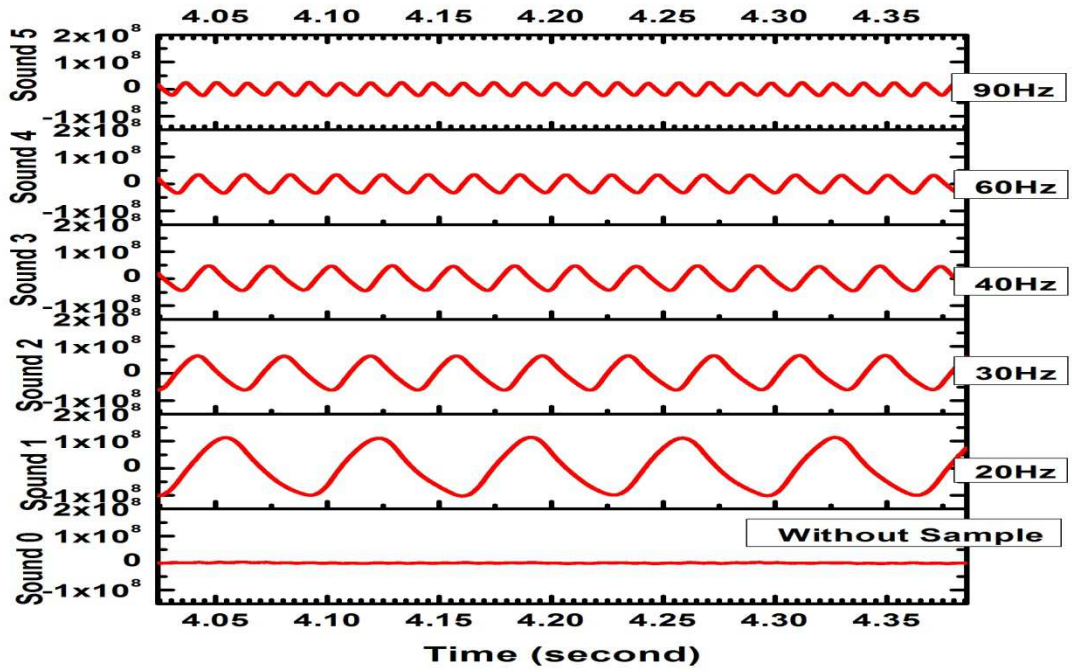

Fig. 9

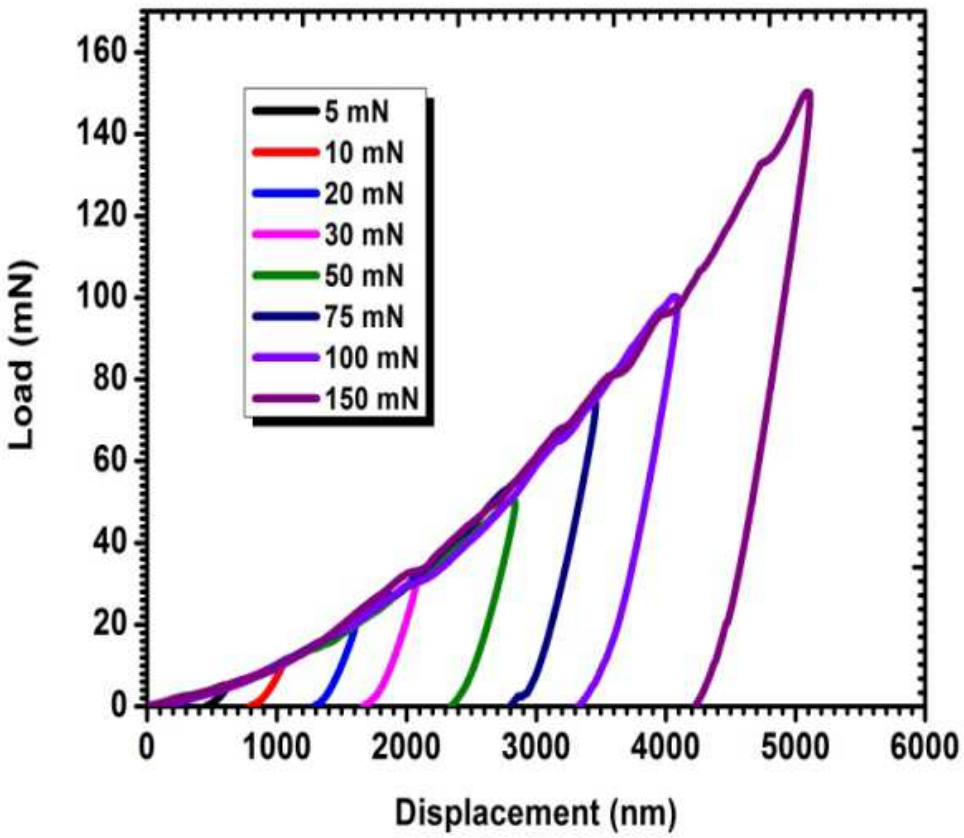

Fig. 10

- LABTF, a nonlinear optical (NLO) crystal was grown by the slow evaporation solution growth technique.
- Iintermolecular hydrogen bonds present in the crystal was discerned using 3D Hirshfeld surface analysis.
- The relative involvements of these interactions are disintegrated using 2D fingerprint plots
- The shock strength above which the crystal induces damage was found by the shock damage threshold technique
- Nanoindentation technique was used to calculate its mechanical parameters.